EEET ECOLOGICAL ENGINEERING & ENVIRONMENTAL TECHNOLOGY

Ecological Engineering & Environmental Technology, 2026, 27(3), 272–289
https://doi.org/10.12912/27197050/218151
ISSN 2719–7050, License CC-BY 4.0

Received: 2026.01.25
Accepted: 2026.02.23
Published: 2026.03.01

Green exploration for hydrothermal alterations and mineral targeting via selective principal component analysis on ASTER data: A case study from the northern Siroua Massif, central Anti-Atlas, Morocco

Abdelhay Ben-Tami[1,4*], Said Belkacim[1], Alvaro. P. Crósta[2], Bouchra Baidada[3], Mohamed Bhilisse[4]

[1] Laboratory of Applied Geology and Geo-Environment, Faculty of Sciences, Ibn Zohr University, Agadir, B.P.8106, Morocco
[2] Geosciences Institute, State University of Campinas, Rua Carlos Gomes, 250 Campinas, 13083-855, SP, Brazil
[3] Higher School of Technology, Fkih Ben Salah, 23200, Sultan Moulay Slimane University, Beni Mellal, Morocco
[4] Zgounder Millennium Silver Mining, Aya Gold and Silver Group, Rue de L'épargne, Quartier Racine, Casablanca, Morocco
* Corresponding author's e-mail: abdelhaybentami@gmail.com

ABSTRACT

Located in northern Siroua, the study area contains mostly magmatic and sedimentary rocks ranging from Neoproterozoic to recent. We applied the principal component analysis (PCA) to selected subsets of four ASTER bands covering the visible-near infrared (VNIR), shortwave infrared (SWIR), and thermal infrared (TIR) spectral ranges to detect minerals of argillic (kaolinite-alunite), phyllic (illite), propylitic (epidote-chlorite-calcite), and potassic (quartz-K-feldspar) alteration associated with the Au-Ag-Cu-Mo-Pb-Zn mineralization and establish relationships with the host rocks in the Zgounder mine and Imourkhssen areas. Results demonstrate that integrating this approach with targeted fieldwork and laboratory studies proved effective in delineating new mineralization prospects. Hence, it provides cost-efficient means for initializing comprehensive exploration programs in high-relief, arid terrains with similar geological settings.

Keywords: ASTER, hydrothermal alteration, principal component analysis, Siroua Massif, Zgounder mine, Imourkhssen

INTRODUCTION

The world's expanding population and economic growth causes an increase in the demand for mineral resources. Therefore, traditional geological mapping and mineral exploration techniques that relies heavily on fieldwork and demand physical processing of rocks may not be the most adequate approach any more, particularly in inaccessible and high-risk terrains. Thus, there is a need for specialized and suitable techniques such as remote sensing in order to overcome these restrictions, minimize source time investment, and therefore locate high-potentially mineralized zones.

Over the last few decades, number of studies highlighted the importance of remote sensing images for both lithological mapping, and detection of hydrothermal alteration areas and structural analysis on porphyry copper and metal-bearing epithermal deposits (Kalkhoran et al., 2025: Laiche et al., 2025; Orynbassarova et al., 2025). Moreover, remote sensing data were also used in land surface climatology studies, vegetation, and ecosystem dynamic studies (Feng et al., 2025). In addition, these techniques proved their high applicability in characterizing the mineralogy of mine wastes and evaluating waste impacts on biologic and hydrologic systems (Guglietta et al., 2025).

The principal component analysis (PCA) technique is a multivariate statistical algorithm employed to enhance and separate certain spectral signals from background noise. It aims at bringing as much as possible of the input signal into orthogonal (uncorrelated) new variables named principal components. As such, it can be applied to spectral bands. Hence, the probability of determining a unique principal component for a single mineral class will increase if the number of input channels is lowered to prevent a particular spectral contrast (Zerai et al., 2023).

In the framework of modern sustainable exploration, this study adopts a green, non-invasive methodology by applying ASTER satellite imagery to characterize hydrothermal alteration. Unlike traditional high-impact field techniques, the application of remote sensing allows for the delineation of alteration and mineralization footprints without surface disturbance. This low-impact technological approach serves as a vital first step in sustainable resource management, minimizing the environmental imprint of the early-stage exploration phase while optimizing target selection through advanced digital processing.

The Siroua Massif has historically served as a cornerstone of the regional economy via its mining sector. Given its extreme aridity and lack of vegetation, the region offers an optimal environment for geological remote sensing. This study leverages these conditions to evaluate the efficiency of advanced spaceborne thermal emission and reflection radiometer (ASTER) data in delineating hydrothermal alteration zones. Consequently, the primary objective of this research is to identify new high-potential exploration targets by mapping hydrothermal alteration assemblages associated with mineralized zones. To achieve this, the investigation focuses on the capability of the principal component analysis (PCA) technique in detecting hydrothermal altered areas with potential for mineralization, and establish their relationships with the host rocks in the Zgounder Mine and Imourkhssen areas. The remote sensing outputs were validated through a multi-proxy approach, integrating field observations with petrographic and geochemical data to confirm the spatial and mineralogical representativeness of the identified alteration zones.

GEOLOGY OF THE SIROUA MASSIF

According to the 1/50,000-scale geological mapping of the Assarrag, Siroua, and Tachoukacht sheets, the Siroua Massif is categorized into several distinct lithostratigraphic units (Thomas et al., 2002, 2004). First, the Paleoproterozoic basement comprises the oldest formations, appearing as altered outcrops of gneiss and schist within the Zenaga Complex (Thomas et al., 2002). Neoproterozoic sequences include the Taghdout Group, deposited on a cratonic margin (Bouougri and Saquaque, 2004), and the ophiolitic Bleida Group, which contains mafic-to-intermediate volcanic successions related to the breakup of Rodinia (Thomas et al., 2002; 2004; Hodel et al., 2020). Second, the Saghro Group is characterized by turbidites and pillow basalts (Thomas et al., 2002). While Saghro Group was previously linked to syn-rift phases (Gasquet et al., 2005), recent U-Pb detrital zircon dating constrained its maximum depositional age to approximately 612–604 Ma (Abati et al., 2010; Errami et al., 2021a). Third, the subsequent Bou Salda Group (c. 610–580 Ma) represents the volcano-sedimentary infills of grabens within the Anti-Atlas Major Fault (AAMF) (Gasquet et al., 2008). Finally, the Ouarzazate Group (580–541 Ma) dominates the post-collisional landscape, consisting of high-K calc-alkaline volcanics and granitoids divided in the Siroua inlier into four subgroups (Tiouin, Bouljama, Tafrant, and Achkoukchi) (Thomas et al., 2004). These are locally overlain by Cambrian sedimentary sequences of the Taroudant Group (Alvaro et al., 2014).

GEOLOGY OF THE SUB-STUDY AREAS

The Zgounder mine

The Zgounder Ag-Hg mine is located on the northwest flank of Siroua Massif, in the central Anti-Atlas Mountains, approximately 260 kilometers east of Agadir city (GPS: 30°45’44”N; 7°44’35”W; alt. 2000 m). Rocks of different types, compositions and ages ranging from Neoproterozoic to Neogene host the deposit (Pelleter et al., 2016) (Fig. 2). The oldest rocks belong to the Saghro Group (Thomas et al., 2002), and comprise sedimentary sequences with intercalated volcanic rocks of basaltic and andesitic compositions. The Bou Salda Group (610–580 Ma) (Gasquet et al., 2008) consists predominantly of the intrusive Tadmant rhyolite which in turn is overlain by the Ouarzazate Group (580–541 Ma) (Thomas et al., 2002). The Miocene volcanic rocks of Siroua overlie the whole assemblage in the eastern part of the mine.

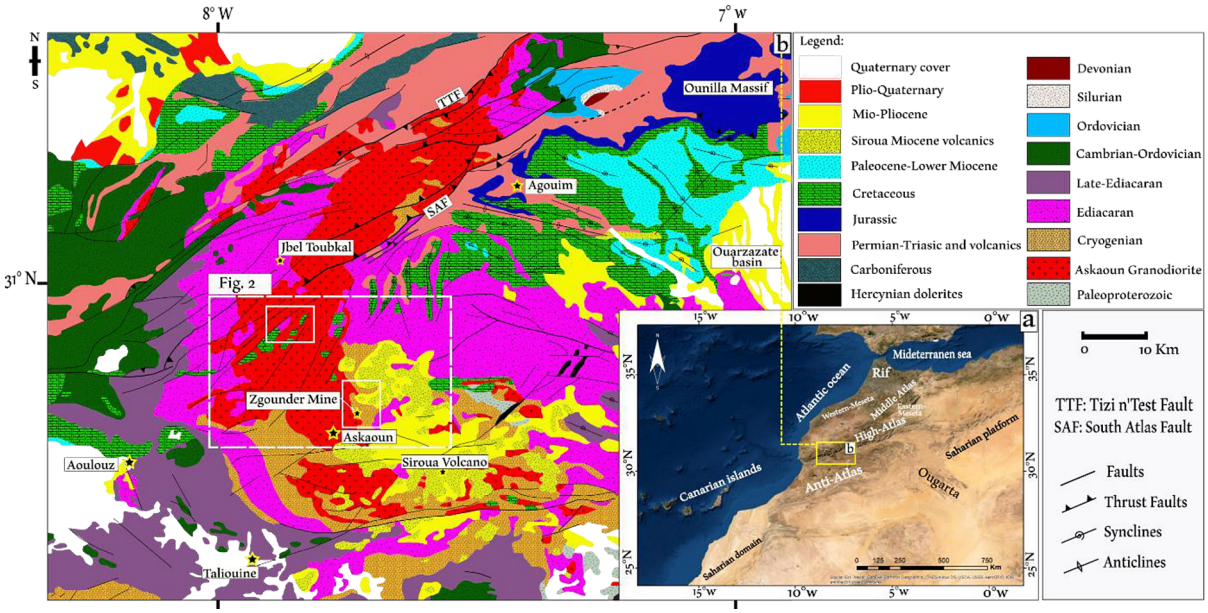

Figure 1. (a) Satellite image of northwest Africa showing the location of Siroua Massif; (b) map of Siroua (redrawn and modified after Oukassou, (2013) with details of the two study areas (Fig. 2)

The Imourkhssen Cu-Mo±Au occurrences

The Imourkhssen Cu-Mo±Au mineral occurrences are located NW of Siroua Massif in the Ouzellagh Siroua promontory in the central Anti-Atlas, covered by the 1/50 000 sheet of Assarrag (Thomas et al., 2002) (Fig. 1). According to Toummite et al., (2013), the high-K calc-alkaline plutonic rocks from the Ouarzazate Group (580–541 Ma) are the most important rocks in the area. These plutonic rocks are represented by Ediacaran granites represented by three suites, namely the Assarrag suite (Askaoun and Tamtattarn pluton), the Amassine suite (Imourkhssen pluton) and the Ougougane suite (small late intrusions) (Fig. 2). Eventually, these rocks are mostly connected with the mineral occurrences previously reported, including Au, Ag, Cu, Pb, Mo, Zn, Hg, Mn, U, and Ba (Belkacim, 2014) (Fig. 2).

MATERIALS AND METHODS

Advanced spaceborne thermal emission and reflection radiometer

The advanced spaceborne thermal emission and reflection radiometer is an advanced multispectral satellite imaging with moderate to high spatial resolution that operated in Earth's orbit (at 705 km) on the first platform of NASA's earth observing system (Terra), starting in June 1998 (Abrams, 2000). The detection of specific alteration assemblages becomes feasible with ASTER in comparison to previous existing multispectral sensors, such as Landsat TM and ETM+. The instrument is capable of capturing an area of 60×60 km in a single image and it is equipped with 14 bands (Wambo et al., 2020). Spectrally positioned at some key portions of the electromagnetic spectrum, as shown in Table 1.

Data acquisition and pre-processing

One ASTER scene acquired on May 12, 2001, was used in the present study. The image has 0% cloud coverage and was obtained from the MADAS (METI AIST Data Archive System) satellite archive. ASTER data imagery can be processed using a variety of image processing techniques. The aim of pre-processing is to reduce the negative effects of the atmospheric interactions, as well as the presence of clouds, vegetation and snow. We proceeded with the techniques described next.

A pre-processing procedure to minimize a spurious effect known to affect ASTER data, named 'cross-talk effect', was applied following the procedure done by (Chattoraj et al., 2020). The cross-talk correction technique aims to improve the spectral separation performance of SWIR data by regulating the amount of stray light and its influence region (Iwasaki and Tonooka, 2005). Then, radiometric calibrations following cross-talk

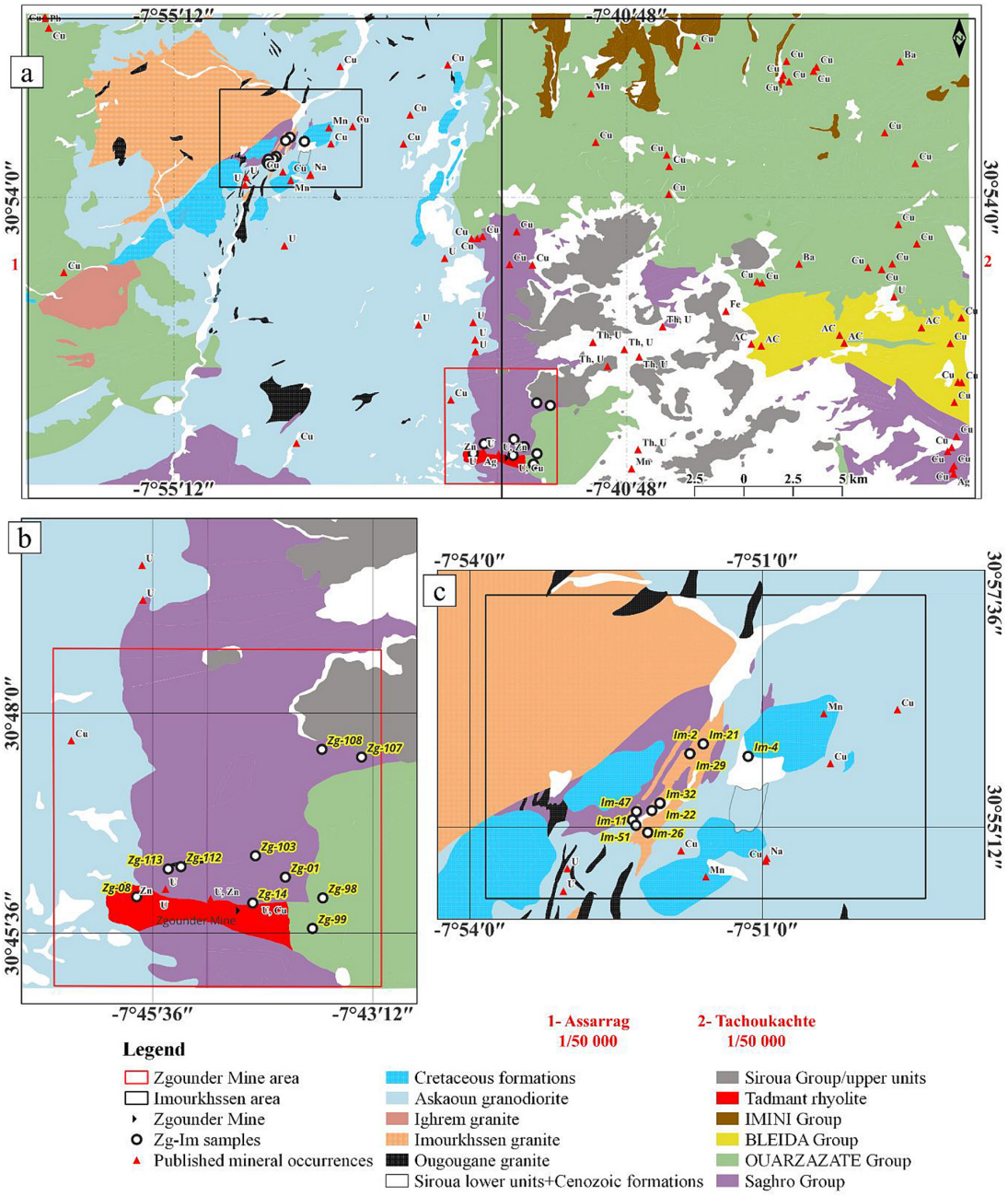

Figure 2. Geological map of the Siroua Massif, based on the 1/50 000 sheets of Assarrag (1) and Tachoukacht (2), with a zoom into the two study areas in b, and c. On the map, Cu: copper; Mn: magnesium; Na: sodium; Ag: silver; Zn: zinc; AC: chrysotile asbestos; U: uranium; Th: thorium; Pb: lead; Ba: barite). Details on the geology and mineral occurrences are from Thomas et al. (2002)

correction have been applied to the data. As atmospheric corrections are critical in the processing of remotely sensed image data, especially, when it comes to spectral analysis on a pixel basis, the next step in data processing was to apply the fast line-of-sight atmospheric analysis of spectral hypercube (FLAASH) algorithm to the VNIR and SWIR datasets (Anderson et al., 2002). For the TIR bands, the thermal atmospheric correction was applied (Wambo et al., 2020; Bakardjiev and Popov, 2015). The sharpening of ASTER subsystems was done by applying the nearest neighbor resampling method in order to resample them to correspond to the SWIR subsystems with 30 m resolution.

Spectral data characteristics

Many minerals exhibit diagnostic absorption features throughout the visible and near infrared (VNIR), shortwave infrared (SWIR), and (or) the

Table 1. ASTER performance parameters and technical characteristics

Sub-system	Band number	Spectral range (μm)	Spatial resolution	Absolute accuracy (σ)	Signal quantization level	Radiometric resolution
VNIR	B1	0.52-0.60	15m	≤ ± 4%	8 bits	NE Δρ ≤ 0.5%
	B2	0.63-0.69				
	B3N (nadir pointing view)	0.78-0.86				
	B3B (backward pointing view)	0.78-0.86				
SWIR	B4	1.600-1.700	30m	≤ ± 4%	8 bits	NE Δρ ≤ 0.5%
	B5	2.145-2.185				NE Δρ ≤ 1.3%
	B6	2.185-2.225				NE Δρ ≤ 1.3%
	B7	2.235-2.285				NE Δρ ≤ 1.3%
	B8	2.295-2.365				NE Δρ ≤ 1.0%
	B9	2.360-2.430				NE Δρ ≤ 1.3%
TIR	B10	8.125-8.475	90m		12 bits	NE ΔT ≤ 0.3k
	B11	8.475-8.825		≤ 3 K (200– 240 K)		
	B12	8.925-9.275		≤ 2 K (240– 270 K)		
	B13	10.25-10.95		≤ 1 K (270– 340 K)		
	B14	10.95-11.65		≤ 2 K (340– 370 K)		
ASTER satellite mass					406 kg	
Altitude orbit					705 km	
Swath Width					60 km	
Total coverage in cross-track direction (Off-nadir pointing)					232 km	
Peak data rate					89.2 Mbps	
Peak power					726 w	
First launched date					June 1998	
Mission life					5 years	

thermal infrared (TIR) regions of the electromagnetic spectrum. We applied the shortwave infrared (SWIR) bands (1000–2500 nm) for mapping argillic, phyllic and propylitic alteration mineral assemblages. Moreover, the thermal infrared (TIR) data are effective for mapping rock types containing quartz and feldspars; minerals that lack distinguishing VNIR + SWIR absorption properties (Rowan et al., 2006).

The common minerals in the argillic alteration, such as alunite and kaolinite, have Al-OH absorption features at 2.17- and 2.20 μm (Rowan et al., 2006), and can be identified by band (5) and band (7) due to another absorption feature of kaolinite centered between 2.235 and 2.285 μm (Madani and Emam, 2011). In addition, the Al-OH absorption of kaolinite is also emphasized employing band (6) (2.185–2.225 μm) due to alteration products of K-feldspar (Pour et al., 2017). Illite, typical in phyllic alteration, has a prominent absorption feature of Al-O-H at 2.20-μm which is uniquely captured by ASTER Band 6. Illite also displays a secondary, less intense absorption feature in the 2.35–2.38 μm range, and can be detected by implementing ASTER band 8 (Mars and Rowan, 2006).

The propylitic alteration is dominated by epidote, calcite, and chlorite. Chlorite and epidote have a Mg-O-H 2.32 μm absorption feature and a broad Fe^{2+} feature from 0.6 to1.65 μm (Neal et al., 2018). Calcite has a prominent feature at 2.33 μm due to CO_3. Epidote, and calcite are easily detected by ASTER band (8) (2.295–2.365 μm) due to Mg-O-H and CO_3 absorption features (Pour et al., 2017 and references therein). These minerals have higher reflectance in bands 7 and 9 (Pour and Hashim, 2012).

The potassic alteration is expressed by quartz+K-feldspar (Ninomiya and Fu, 2016). Quartz is characterized by strong emissivity minima in band 10 (approx. 8.3 μm) and band 12 (approx. 9.1 μm). In contrast, it shows higher emissivity in band 11 (8.6 μm) 14 (11.3 μm). K-Feldspar exhibits an emissivity minimum in band 11. This distinct emissivity minimum facilitates

the spectral discrimination of K-feldspar from quartz within felsic lithologies.

Mineral endmember identification using PCA of ASTER bands

In this study, only specific bands that contain contrasting absorption and reflection features of the target minerals are chosen. The PCA algorithm was applied to subsets of four ASTER bands to map the distribution of some alteration minerals. Thus, minerals like illite is representative of phyllic alteration zone; kaolinite and alunite are typical of argillic alteration; chlorite and epidote are representative of propylitic alteration. Moreover, a subset of four ASTER TIR bands was used for mapping potassic alteration.

To the extent of this study, four sets of ASTER bands were chosen for each targeted alteration mineral in accordance with established literature. As detailed in Table 2, these bands were chosen to capture diagnostic spectral features, with negative eigenvector loadings (–) assigned to represent absorption bands and positive loadings (+) assigned to represent reflectance bands.

After performing PCA on the selected band subsets, an examination of the eigenvector loadings is required to identify which PC image contains the spectral information related to specific target minerals. In accordance with the Crosta technique, the representative image for a target mineral is identified as the principal component (PC) exhibiting the highest magnitude eigenvector loadings within the diagnostic ASTER bands. Ideally, the optimal PC must show opposing signs (one positive and one negative) between the bands representing the mineral's spectral absorption/reflection bands, thereby maximizing the spectral contrast required for effective mapping (Crósta et al., 2003).

The optimal Principal Component (PC) for mineral mapping was identified using the feature-oriented principal component selection (FPCS) framework, originally proposed by Crósta and Moore, (1989) and further refined for multispectral sensors by Loughlin, (1991). This method identifies the PC that maximizes the statistical variance between the diagnostic reflection and absorption bands of a target mineral.

The decision index (D) for each PC was calculated by multiplying the eigenvector loading (L) by the corresponding spectral signs (S) for each band following this formula:

$$D = \sum_{i=1}^{n} (L_i \times S_i) \quad (1)$$

where: L_i represents the eigenvector loading for band i, S_i is the sign of spectral response (defined as +1 for reflection bands and -1 for diagnostic absorption bands, as detailed in Table 2.

The PC yielding the highest absolute value (D) was identified as the most representative for the target mineral. To ensure a consistent visualization where mineral anomalies appear as bright pixels (high values), the following sign convention was applied

- If (D) is negative (–), the PC image maps high mineral concentrations as bright values; no further processing is required.
- If (D) is positive (+), the PC image is multiplied by (-1) (negated) to invert the greyscale and highlight the mineralized zones as bright anomalies.

Ground validation and sampling strategy

Selection criteria and sampling protocol

The sampling protocol was primarily executed within the two focal study areas as part of a regional exploration initiative funded by the Zgounder Millennium Silver Mining Company

Table 2. Selective bands and their correspondence with an absorptive (–), or reflective (+) feature for each targeted alteration mineral

Band	1	3	4	5	6	7	8	9	10	12	13	14
Alunite	-	+		-		+						
Kaolinite	-		+		-	+						
Illite	+	-		+	-							
Chlorite+epidote	-					+	-	+				
Carbonates (calcite)	-		+				-	+				
Quartz+K-feldspar									-	-	+	+

(ZMSM). While certain adjacent areas exhibited high spectral interest, they were excluded from the validation campaign as they fall within the active exploration permits held by third-party companies. Consequently, while the sampling is done within the accessible zones, the overall spatial representativeness was constrained by legal and jurisdictional boundaries.

After field sampling, laboratory examinations were conducted on the collected samples from the two sub study areas, particularly on samples from the inferred hydrothermal alteration zones, in order to validate the above produced alteration images. Thus, for the petrographical and mineralogical studies; the different textures and mineral assemblages were studied at the laboratory of the Faculté des Sciences, Université Ibnou Zohr, Agadir, Maroc. For the geochemical analysis, a total of 25 grab samples were collected in in both the Zgounder Mine and Imourkhssen areas. They were then analyzed for their contents in Au, Ag, As, Co, Cu, Fe, Mo, Ni, Pb, and Zn.

Geochemical analysis of samples from the Zgounder Mine area were carried out at the Activation Laboratories. Ltd (Actlabs) (Ancaster, Ontario, Canada), while samples from the Imourkhssen area were analyzed at the National Office of Hydrocarbons and Mines laboratory (ONHYM) (Rabat, Morocco) (Table 9).

RESULTS

The argillic alteration

Kaolinite

For mapping kaolinite, the examination of the eigenvector statistics for the ASTER bandset used (Table 3), shows that PC4 has a high and positive loading from band 7 (0.670779), and high and negative loading from band 1 (-0.530501). The reason is that kaolinite has high reflectance in bands 4 and 7, with high absorbance in band 6. Also, as the values for bands 1 and 6 are both negative, and the values for band 4 and 7 are both positive, this is a very good case for a kaolinite abundance image. Lastly, the loading for the absorption band 6 is negative (-0.41794), kaolinite will appear as bright pixels in the PC4 image after negation (multiplied by -1).

Alunite

Alunite has a high absorbance in ASTER bands 1 and 5, and high reflectance in bands 3 and 7. The PCA results for alunite (Table 4) show that PC3 has a high and negative loading from band 7 (-0.701551) and high and positive loading from band 1 (0.525498). As these contributions are positive for band 1, and negative for bands 3 and 7, the resulting PC will depict alunite-bearing pixels in dark tones (low DNs). For clear visualization, the original PC3 image was multiplied by – (1), thus inverting the grey levels so that the target mineral appears as bright pixels in the abundance image (Fig. 2). Bands 3 and 7 for alunite have negative values, but bands 1 and 5 have both positive and negative values in PC3 (0.525498 and -0.125161 respectively). However, as its eigenvector loading for band 5 (-0.125161) is much lower than the loading of the other 3 bands, its interference in the final PC3 alunite abundance image is negligible.

The phyllic alteration

Illite

To map illite-related phyllic alteration, the eigenvector matrix of the selective PCA (bands 1, 3, 5, 6) was analyzed (Table 5). Although PC3 accounted for a higher decision index (1.558369) (see Supplementary Table), it was rejected for mineral targeting due to lack of sign inversion between reflective and absorptive bands. PC4 however was identified as the optimal illite abundance

Table 3. Eigenvector loadings for 4 bands of ASTER for kaolinite

Bands	PC				Alteration mineral
	PC1	PC2	PC3	PC4	
Band 1	-0.423104	-0.529538	-0.509059	-0.530501	Kaolinite
Band 4	-0.905103	0.279792	0.237634	0.214556	
Band 6	0.037780	0.799014	-0.370891	-0.471794	
Band 7	-0.018541	0.053697	-0.739479	0.670779	

Table 4. Eigenvector loadings for 4 bands of ASTER data for alunite

Bands	PC				Alteration mineral
	PC1	PC2	PC3	PC4	
Band 1	0.453550	0.479042	0.525498	0.537274	Alunite
Band 3	0.678010	0.361453	-0.464772	-0.440047	
Band 5	-0.578408	0.799580	-0.125161	-0.102227	
Band 7	-0.006253	-0.023283	-0.701551	0.712212	

image. It fulfills the Crósta Technique criteria by exhibiting the highest loading on the absorptive band 6 (+0.718443) with an opposing sign to the reflective band 5 (-0.096933). This configuration successfully isolates the Al-OH absorption feature unique to illite. Because the absorptive band 6 is positively loaded, illite-rich pixels were initially displayed as dark values; consequently, the image was negated (multiplied by -1) to represent high illite concentrations as bright pixels for final visualization.

The propylitic alteration

Chlorite+epidote

Chlorite, and epidote are characterized by high reflectance in bands 7 and 9, with absorption features in band 8. PC3 of ASTER bands of 1, 7, 8 and 9 (Table 6) shows high and positive values in band 9 (0.814054), and negative values in band 8 (-0.033295). Moreover, band 1 also exhibits a high and a negative loading (-0.526999), and using it can help suppressing background albedo and vegetation, further isolating the specific spectral response of the alteration minerals. Overall, bands 7 and 9 of ASTER in which minerals related to propylitic alteration reflects energy have both positive values, and bands 1 and 8 in which these minerals absorb energy have both negative values. Therefore, the resulting abundance image will depict chlorite+epidote bearing-pixels as bright tones (Fig. 4).

Calcite

PC4 of the band subset of 1, 4, 8 and 9 (Table 7) shows high and positive loading from band 9 (0.620102), and high and negative one for band 1 (-0.508065). In detail, the two bands 4 and 9 in which carbonates reflect more energy have both positive values, contrarily to band 8 in which carbonates absorb more energy that have negative values. Therefore, the resulting abundance image highlights carbonate-bearing pixels in bright tones (Fig. 4).

The potassic alteration

Quartz+K-feldspar

For mapping potassic alteration, a four ASTER TIR band subset was used as input for PCA (Table 8). Typically, potassic alteration minerals like quartz show high absorption in ASTER bands 10 and 12, and high reflectance in bands 13 and 14. while PC1 contains the most statistical information (Decision index = 1.829562) (see Supplementary Table); it is generally considered the "noise" or background component when using the Crosta technique for targeted alteration mapping. PC2 however, with its specific opposing signs, is the correct component for isolating the subtle spectral signature of quartz/silicification. PC2 shows high and negative loadings for band 14 and 13 (-0.721943, and -0.463863 respectively), and high and positive ones for bands 10 and 12 (0.502962, 0.103243 respectively). In

Table 5. Eigenvector loadings for 4 bands of ASTER data for illite

Bands	PC				Alteration mineral
	PC1	PC2	PC3	PC4	
Band 1	0.458730	0.484952	0.532054	0.520871	Illite
Band 3	0.673796	0.356421	-0.464571	-0.450707	
Band 5	-0.579157	0.798357	-0.133443	-0.096933	
Band 6	0.011979	-0.020278	-0.695187	0.718443	

Table 6. Eigenvector loadings for 4 bands of ASTER data for chlorite+epidote

Bands	PC				Alteration minerals
	PC1	PC2	PC3	PC4	
Band 1	-0.427661	-0.530302	-0.526999	-0.508093	Chlorite+epidote
Band 7	-0.903819	0.245383	0.241828	0.253807	
Band 8	0.012503	-0.679299	-0.033295	0.733000	
Band 9	-0.007852	-0.443983	0.814054	-0.374345	

Table 7. Eigenvector loadings for 4 bands of ASTER data proposed for calcite.

Bands	PC				Alteration mineral
	PC1	PC2	PC3	PC4	
Band 1	-0.432015	-0.525009	-0.528771	-0.508065	Carbonates (calcite)
Band 4	0.901475	0.275030	0.237772	0.234873	
Band 8	0.024809	0.788435	-0.274914	-0.549707	
Band 9	0.009480	0.164605	-0.767000	0.620102	

this sense, the resulting PC2 will exhibit silicified alteration as bright pixels after inverting PC2 grey levels by multiplying it by – (1) (Fig. 4).

A summary of the results achieved with the PCA method for argillic (alunite and kaolinite) and phyllic (Illite) alteration are presented in Figure 3 as an RGB abundance image draped over ASTER band 3. The resulting abundance image for the propylitic alteration minerals (calcite-chlorite+epidote), and potassic alteration minerals (quartz+K-feldspar) is shown in Figure 4 as an RGB image of these three minerals and draped over ASTER band 3.

DISCUSSION

Figure 3 represent the results of PCA method of the argillic and phyllic alterations. For the argillic alteration; the image reveals the distribution of alunite over the Siroua volcanics (Fig. 3a). In fact, alunite alteration is often associated with volcanic tuffs and phonolites. This association occurs because these rock types provide the necessary chemical components and physical structure for acid-sulfate (advanced argillic) alteration to occur (Hedenquist and Taran, 2013; Bouvart et al., 2024). Kaolinite occurrences are shown in red and are mostly spread over the Siroua volcanics zoning out from the alunite. Normally, alunite often forms the inner core of an alteration zone (the "lithocap"), which can grade outward into kaolinite and then illite/smectite as the fluids become less acidic (Hedenquist and Taran, 2013).

For the phyllic alteration, Illite occurrences show a relatively non uniform patterns. For illite, although PC3 accounted for a higher decision index (1.558369) (see Supplementary Table 10), it was rejected for mineral targeting because both the reflective band 5 and the diagnostic absorption band 6 exhibited negative loadings (-0.133443 and -0.695187, respectively) (refer to Table 5). This lack of sign inversion indicates that PC3 captures common albedo variations rather than the specific spectral contrast of the target mineral. Therefore, PC4 was chosen to highlight illite-rich

Table 8. Eigenvector loadings for 4 TIR bands of ASTER data for the potassic alteration minerals

Bands	PC				Alteration minerals
	PC1	PC2	PC3	PC4	
Band 10	0.496866	0.502962	0.498303	0.501845	Quartz+K-feldspar
Band 13	0.581248	-0.463863	0.415849	-0.523500	
Band 12	-0.633540	0.103243	0.737809	-0.208819	
Band 14	-0.117908	-0.721943	0.185477	0.656121	

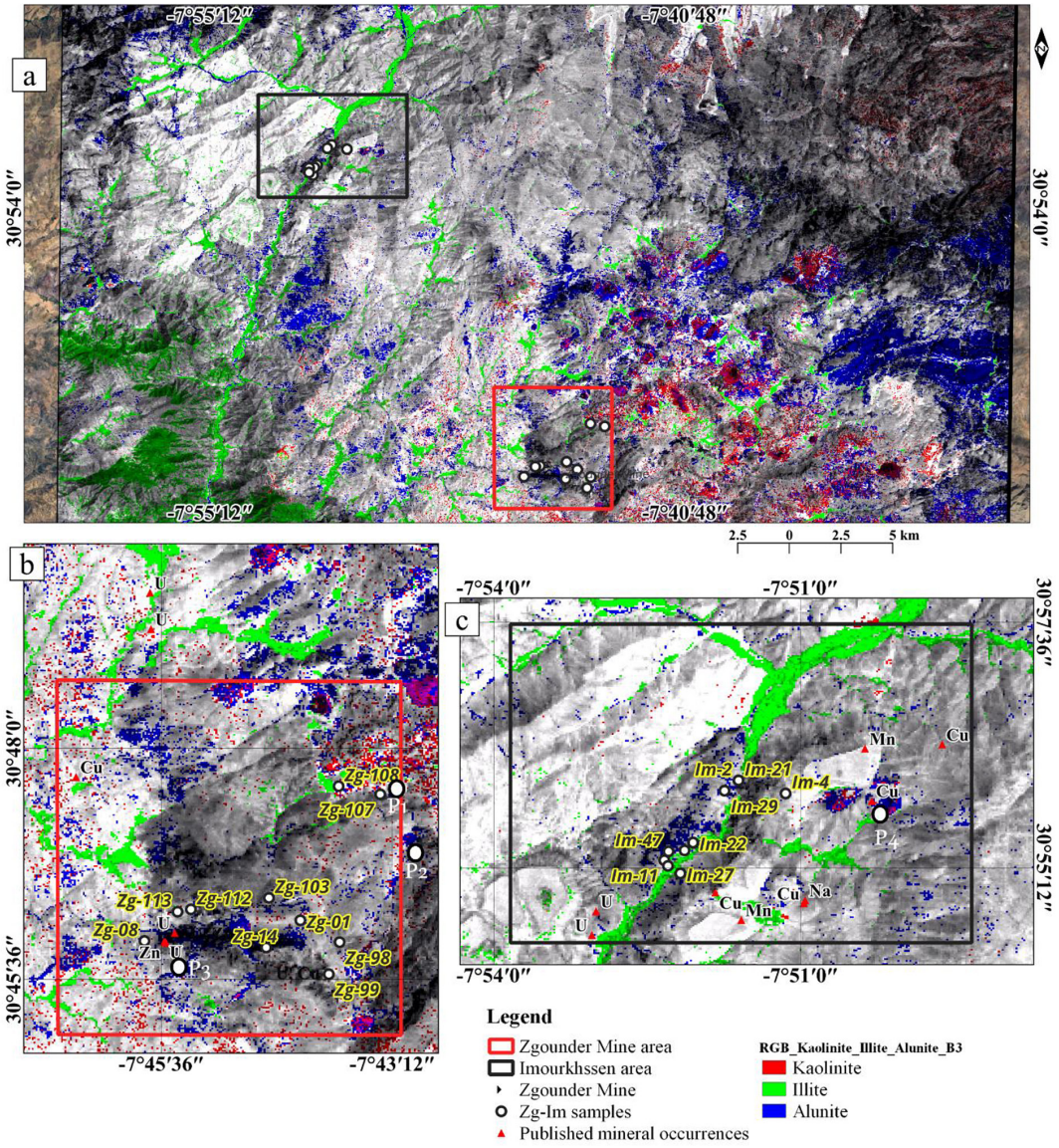

Figure 3. RGB color composite image of alteration minerals for the argillic (alunite-kaolinite) and phyllic (illite), draped over ASTER band 3 for visualization. Mineral occurrences (Cu: copper; Mn: magnesium; Na: sodium; Ag: silver; Zn: zinc; AC: chrysotile asbestos; U: uranium; Th: thorium; Ba: barite; Fe: iron). Refer to Figure 5 for photographs of P1-P4 localities

pixels. On Figure 3a, it is clear that illite looks like highlighting mountain ridges on the low left corner of the map. Eventually, this can be attributed to topographic effects, as mountain ridges provide faces with direct solar exposure, yielding a higher signal-to-noise ratio for spectral identification compared to shadowed or soil-covered slopes.

Figure 4 represents the results of PCA method for the propylitic and potassic alterations. For the potassic alteration; the quartz+K-feldspar assemblage is widely but not uniformly distributed. Specifically, the spatial distribution of this alteration is in accordance with field data, particularly within the Imourkhssen granite in the Imourkhssen area (Fig. 4c). This intrusion is intensely affected by potassic alteration characterized by the presence of flesh-colored K-feldspar into the rock (Fig. 5e, h). Furthermore, the PCA results effectively distinguish the Tadmant rhyolite Formation in the Zgounder Mine area (Fig. 2), along with the associated rhyolite dykes (Fig. 4b).

For the propylitic alteration, its abundance stretches over the Siroua volcanic rocks. This distribution follows a lateral zonation behind the argillic and phyllic alterations (Fig. 4a). In the Zgounder Mine area, well-developed propylitic alteration is visible from the southern part of the Imghi Formation (Fig. 4b). In contrast, the applied PCA does not

depict this alteration for the whole Imghi Formation (e.g., on its southern part; Fig. 4b). The reason for this spectral variability might due to a mixed pixel effect, wherein the presence of active agricultural cover introduces confounding vegetation and soil moisture signatures that obscure the diagnostic absorption features of the target minerals.

FIELD INVESTIGATIONS AND VALIDATION PROTOCOL

According to field observations, the sub-study areas contain considerable levels of argillic, phyllic, propylitic and potassic alterations, along with some silicification (Fig. 5).

Petrographic and mineralogical studies

The petrographic studies carried out on samples from the sub-study areas highlighted the existence of major alteration minerals associated to the inferred alteration zones including minerals like abundant chlorite, kaolinite, sericite, and muscovite (Fig. 6).

Under transmitted light, the three samples taken from the Tadmant rhyolite (Bou Salda Group) in the Zgounder Mine area show all a microcrystalline

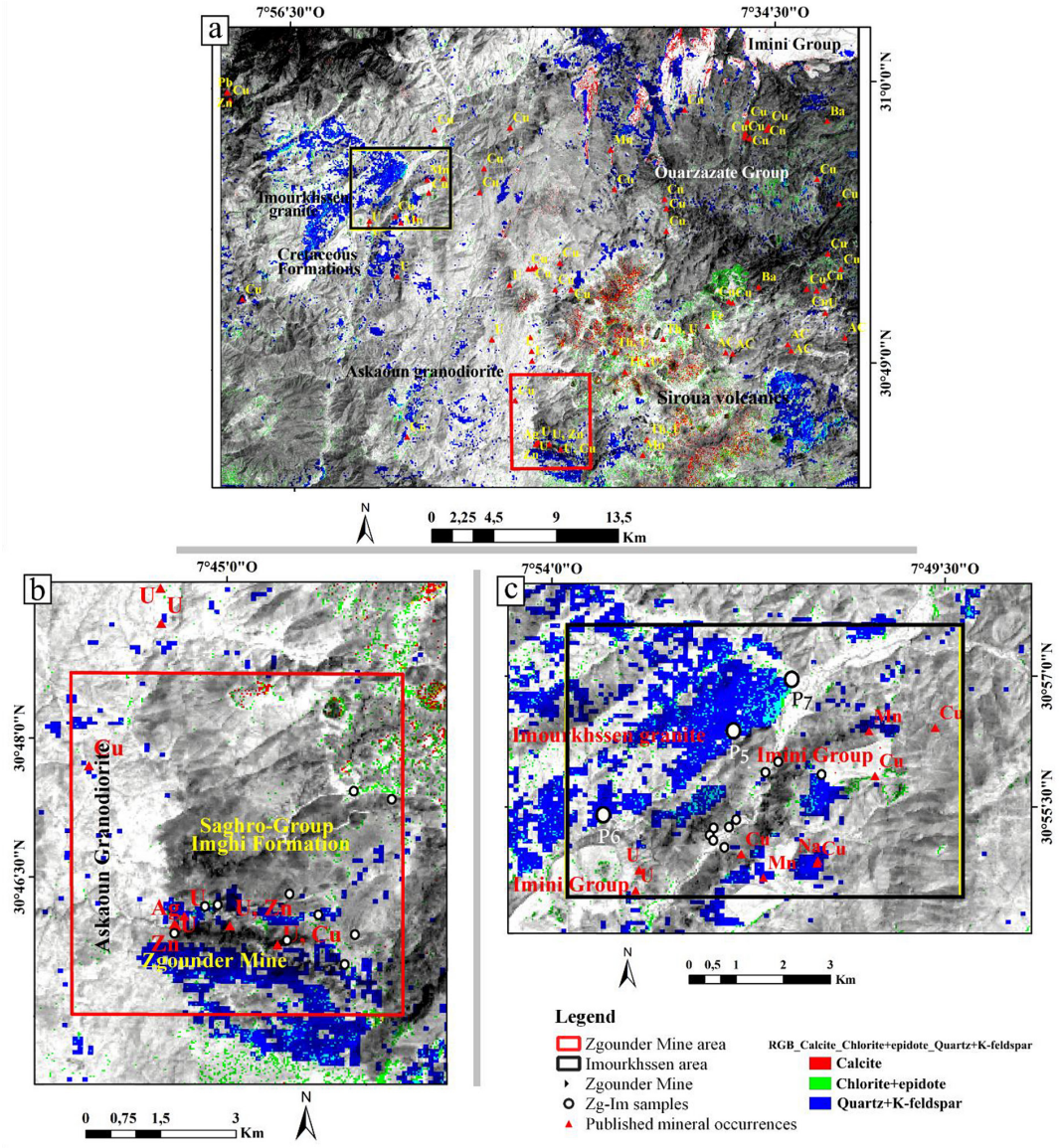

Figure 4. RGB color composite image of alteration minerals for the propylitic (calcite-chlorite+epidote) and potassic alteration (quartz+K-feldspar) draped over ASTER band 3. Mineral occurrences (Cu: copper; Mn: magnesium; Na: sodium; Ag: silver; Zn: zinc; AC: chrysotile asbestos; U: uranium; Th: thorium; Ba: barite; Fe: iron). Refer to Figure 5 for photographs of P5, P6 and P7 localities

porphyritic texture with quartz, K-feldspar altered to albite, and crystallized inside a devitrified matrix. Secondary alteration minerals chlorite, sericite, albite, with some carbonates (Fig. 6a, and Fig. 6b). The meta-dolerite sample (Zg-14) collected from a dolerite dyke next the mineralized zone of the Zgounder Mine have an intersertal texture with interstitial quartz into which phantom laths of black plagioclase were included in the phantom pyroxene crystals (Fig. 6c, Fig. 6d). Between these phantoms, interstitial spaces show a granonematoblastic microcrystalline texture. The plagioclase crystals are strongly altered and replaced by a mixture of chlorite, weak and sparse grains of epidote. Clinopyroxenes are mainly replaced by amphiboles (hornblende and actinolite). The sample contains small ilmenite laths with some being partly replaced by pyrite (Fig. 6c, Figd). The samples of the argillic alteration in the Zgounder Mine area have abundant quartz. The alteration in this zone is manifested by advanced replacement of hydrothermal quartz, plagioclase, and mafic minerals by clays. The fine-grained clay minerals with kaolinite aggregates are wrapped by pyrophyllite replacing hydrothermal quartz. Two generations of chlorite replace former mafic phases. The groundmass is partially silicified and sericitized (Fig. 6e). In addition, clay minerals fill pores and gaps between plagioclase crystals (Fig. 6f). Kaolinite-pyrophyllite in feldspars and sericitized plagioclases are visible in (Fig. 6g). The Bou-Tazart granite/granophyre show a graphic intergrowth boundary of quartz and K-feldspar around quartz phenocrysts (Fig. 6h).

For the Imourkhssen area, the study of samples of the propylitic zone from the Askaoun granodiorite showed the extensive replacement of lath-shaped feldspar phenocrysts by sericite and clay minerals. They are associated to chlorite and iron-oxides (Fig. 6o). Chlorite replaces biotite, with muscovite micro-patches next to chlorite crystals (Fig. 6i, Fig 6j). Petrographic studies of similar zones by Toummite, (2012) identified advanced propylitic alteration within the Askaoun granodiorite. This is characterized by epidote patches analogous to those observed in this study (Fig. 6l). In the

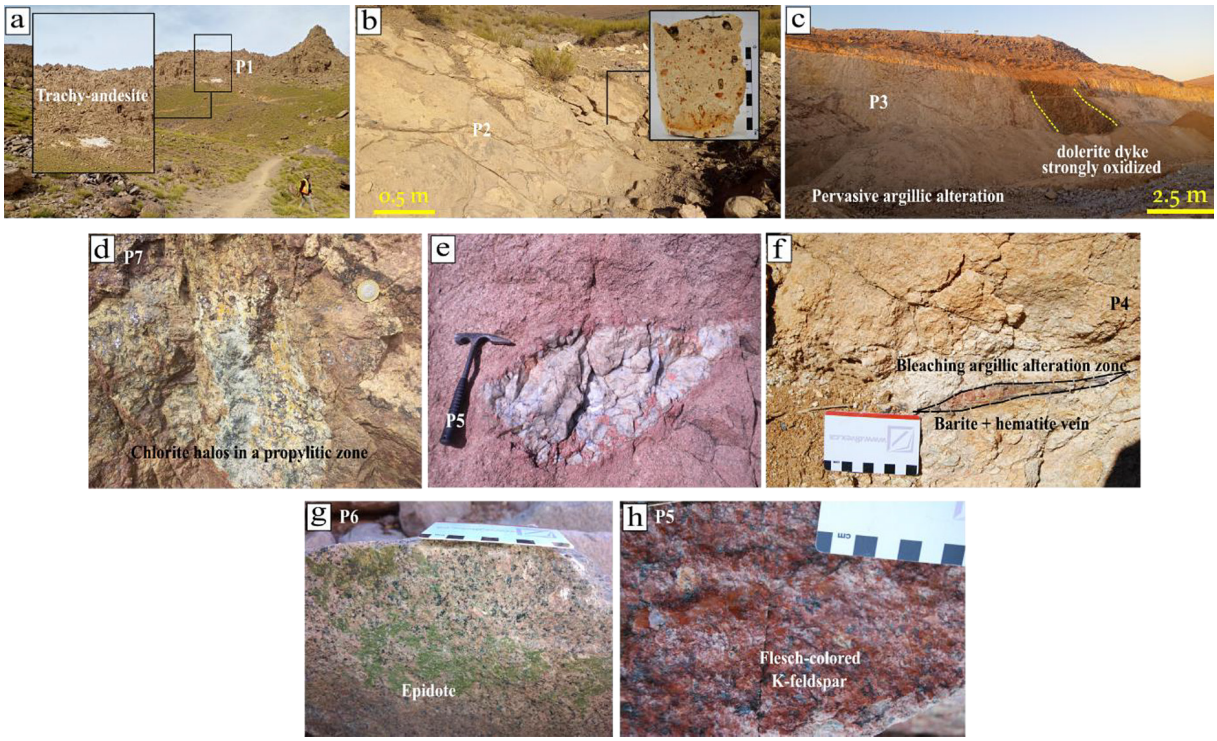

Figure 5. Examples of the surface alteration zones at the Zgounder mine and Imourkhssen areas. (a): strong argillic alteration zone associated to the Neogene trachy-andesites in the Tittalt village. (b): strong argillic alteration affecting the lapilli-tuffs of the Ouarzazate Group. (c): distribution and zoning of alteration zones surrounding the oxidized dolerite dyke, from argillic alteration minerals on the left side of the dyke to the slightly sericitic alteration on the right corner. (d): propylitic alteration zone with halos of chlorite associated with molybdenum mineralization. (e): quartz pocket in highly altered Imourkhssen granite. (f): bleaching of the sericitic-argillic zone with a barite+hematite vein. (g): propylitic alteration with developed epidote in the Imourkhssen granite. (h): flesh-colored K-feldspar within the Imourkhssen granite

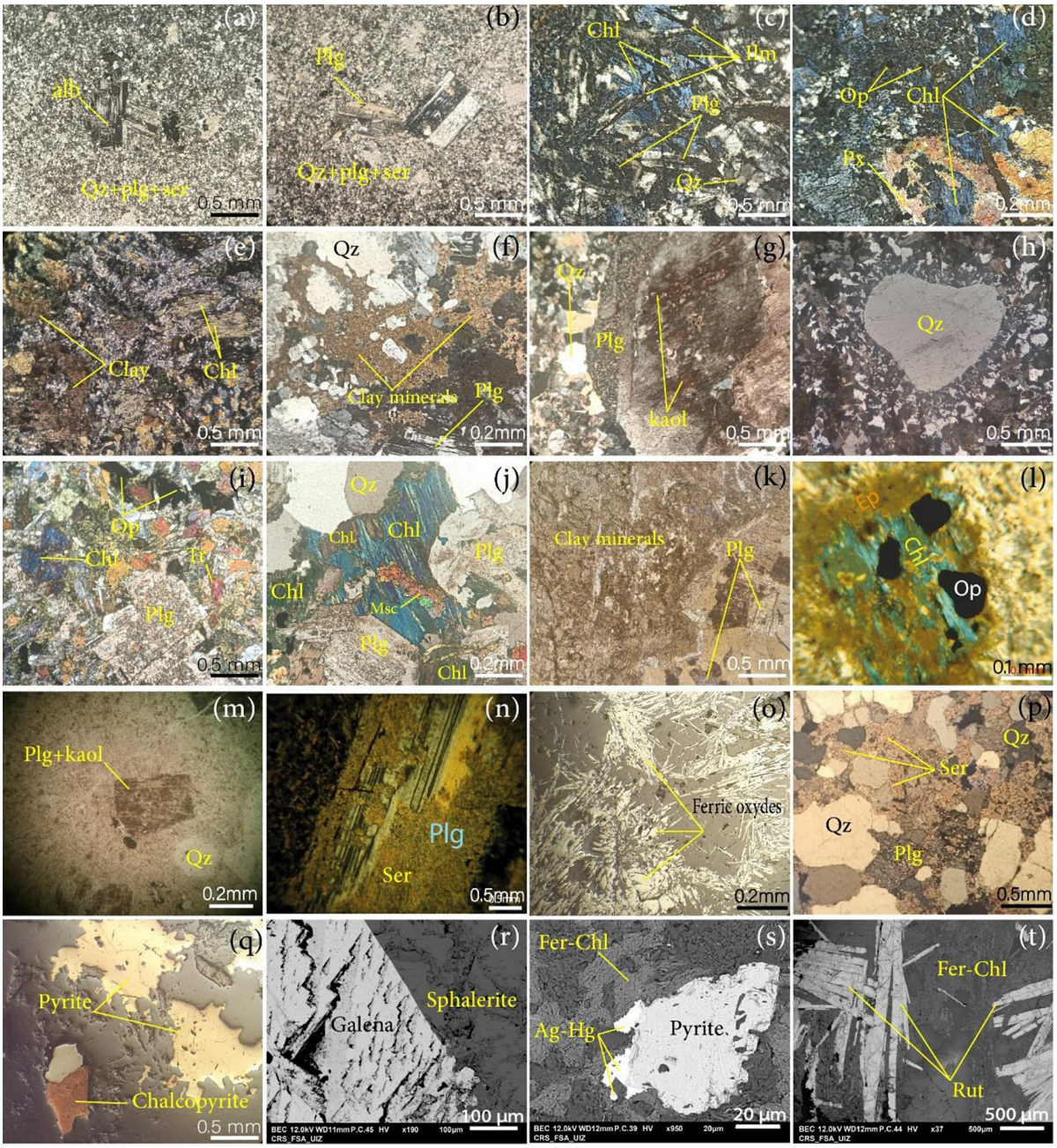

Figure 6. Microphotographs of some hydrothermal alteration features and mineralization occurrences in the Zgounder Mine and Imourkhssen areas (all images taken under the transmitted light microscopy are in the polarized light (a to n + p). (a), (b): microcrystalline porphyritic texture with quartz, K-feldspar altered to albite, and crystallized inside a devitrified matrix (Zg-112, Zg-113). (c), (d): intersertal texture with interstitial quartz exhibiting phantom laths of black plagioclase included in the phantom pyroxene crystals; alteration is marked by well-developed patches of chlorite and sparse grains of epidote (Zg-14). (e): fine-grained clay minerals probably replacing hydrothermal quartz; chlorite replacing former mafic minerals; the groundmass is mostly silicified and sericitized. (f): clay minerals filling pores and gaps between minerals (quartz-plagioclase) in a microgranite. (g): clay minerals (kaolinite wrapped by small patches of pyrophyllite) in the Bou-Tazart granite (Ouarzazate Group) (Zg-99). (h): a graphic intergrowth boundary of quartz and K-feldspar around quartz phenocrysts in the granite/granophyre of the Bou-Tazart (Zg-99). (i), (j): sericitized plagioclase phenocrysts cut by thin veinlets of sericite in the Askaoun granodiorite; chlorite replacing biotite with some micro-patches of muscovite (Zg-08). (k): clay minerals with sericitized plagioclase. (l): epidote and chlorite in a propylitic zone. (m), (n): kaolinitized and sericitized plagioclase. (o): ferric oxide minerals. (p): bleaching sericitic-argillic zone. (q): pyrite-chalcopyrite association in the Imourkhssen area (reflected light). (r): galena and sphalerite association in a sample from the Zgounder Mine area (SEM). (s): Ag-Hg amalgam associated with pyrite and a ferriferous chlorite (SEM). (t): ferriferous chlorite associated with rutile (SEM). Abbreviations: alb: albite; Qz: quartz; Plg: plagioclase; Ser: sericite; Chl: chlorite; Ilm: ilmenite; Op: opaque minerals; Px: pyroxene; Kaol: kaolinite; Tr: Trimolite; Msc: muscovite; Ep; epidote; Fer-Chl: Ferriferous chlorite; Rut: rutile; Ag-Hg: Silver-mercury; SEM: scanning electron microscope

field, the Imourkhssen granite's core is characterized by heavily albitized and potassic alteration, which is highlighted by the development of coarse-grained pink-colored potassium feldspar as veins and veinlets (Fig. 5e, Fig. 5h). This alteration is linked to a molybdenum mineralization according to Belkacim, (2014) (Fig. 5d). Two samples taken from a sericitic-argillic zone show high abundance of clay minerals replacing phenocrysts of feldspar and highly sericitized plagioclase (Fig. 6k, Fig 6m, Fig. 6n). A zone in the Imourkhssen area referred to as a bleaching sericitic-argillic zone (Fig. 5f), shows an assemblage of quartz, plagioclase, sericite and opaque minerals (Fig. 6p). The intense quartz-sericite alteration in this phyllic zone is accompanied by some plagioclase crystals being partially obliterated. However, the co-existence of sericite and secondary quartz might indicate simultaneous sericitic and argillic alteration, plus and silicification, with the sericitic alteration conditioned by the rock fabric and texture.

Polished sections were prepared from representative samples collected within the mineralized zones of the Zgounder Mine and the Imourkhssen areas. Scanning Electron Microscopy (SEM) analysis revealed an abundance of sulfide minerals, including pyrite, chalcopyrite, sphalerite, and galena, along with silver-mercury amalgams. Additionally, ferriferous chlorite and iron oxides were identified within the mineralized assemblage. These mineralogical relationships are illustrated in Figure 6q, 6r, 6s, and 6t. The presence of silver-mercury amalgams and base metal sulfides specifically pyrite, chalcopyrite, sphalerite, and galena provides empirical evidence of metal-saturated hydrothermal fluids. This suggests that the identified alteration halos are genetically linked to a substantial and productive polymetallic mineralizing system.

Geochemical analysis on selected samples from the Zgounder mine and Imourkhssen areas

The geochemical distribution across the two study areas highlights distinct metallic signatures (Fig. 2): in the Zgounder mine area, silver (Ag) and zinc (Zn) concentrations peak in sample Zg-14 (> 100 ppm Ag; 540 ppm Zn), followed by significant zinc levels in sample Zg-107 (270 ppm) and Zg-103 (210 ppm), while copper (Cu) is most elevated in Zg-107 (110 ppm) and Zg-103 (100 ppm). Conversely, the Imourkhssen area displays a gold-copper dominant profile, with sample Im-21 yielding the highest values for gold (29.77 ppb Au), silver (8.69 ppm Ag), and copper (1,439.88 ppm Cu). Secondary copper peaks occur in Im-22 (675.43 ppm), while zinc concentrations in this sector are highest in sample Im-22 (130.30 ppm) and Im-51 (117.35 ppm).

These geochemical results differentiate two distinct mineralizing environments. The Zgounder Mine area is characterized by a high-grade Ag-Zn-As signature, highlighted by extreme silver and zinc enrichment in sample Zg-14, and elevated arsenic in Zg-103, correlating with proximal epithermal alteration. In contrast, the Imourkhssen area reveals a high-temperature Au-Cu-Mo-Co association, featuring massive copper levels in Im-21 and an extreme molybdenum spike in Im-2.

As for the promising contents in gold, silver and copper in the analyzed samples (Table 9). These findings serve as high-priority vectors for future exploration and detailed site investigation. While several mineral occurrences in these sectors have been previously documented (Fig. 2), the geochemical results presented here reinforce the untapped economic potential of these mineralized systems. Furthermore, the alignment of these anomalies with ASTER-derived alteration zones provides a framework for identifying extensions of known deposits and discovering new targets in under-evaluated areas of the Anti-Atlas.

DISCUSSION

The Siroua Massif is renowned for its prolific mineral resources, primarily characterized by multi-scale silver and copper deposits, alongside late-stage barite occurrences. Key among these is the Zgounder Ag-Hg deposit, a world-class epithermal system formed through multi-stage mineralization events linked to Neoproterozoic volcanism and subsequent tectonic reactivation (Marcoux and Wadjinny, 2005; Pelleter et al., 2016). Beyond silver, the region demonstrates significant potential for copper and gold, largely controlled by major Pan-African structural corridors and the complex interplay between late-Ediacaran granitoids and the PIII volcano-sedimentary series (Tuduri et al., 2018). Recent structural and spectral mapping in the Anti-Atlas has emphasized the Siroua region as a critical zone for

Table 9. Contents in Ag, As, Co, Cu, Fe, Mo, Ni, Pb, and Zn for the analyzed samples from the Zgounder Mine and Imourkhssen areas. Abbreviations: NA, not available; Zg, Zgounder; Im, Imourkhssen. Refer to Figure 2 for samples location

Sample code	Longitude	Latitude	Au (ppb)	Ag (ppm)	As (ppm)	Co (ppm)	Cu (ppm)	Mo (ppm)	Ni (ppm)	Pb (ppm)	Zn (ppm)
Zgounder Mine area											
Zg-01	-7.73437	30.76772	NA	1.20	< 5	2.00	20.00	14.00	40.00	5.00	< 30
Zg-08	-7.76137	30.76415	NA	1.60	6.00	17.00	30.00	7.00	40.00	13.00	190.00
Zg-14	-7.74029	30.76302	NA	> 100	49.00	46.00	20.00	3.00	60.00	44.00	540.00
Zg-98	-7.72756	30.76394	NA	31.00	12.00	5.00	30.00	15.00	30.00	8.00	< 30
Zg-99	-7.72944	30.75840	NA	0.80	11.00	6.00	40.00	13.00	30.00	8.00	60.00
Zg-103	-7.73980	30.77161	NA	0.50	50.00	51.00	100.00	9.00	100.00	24.00	210.00
Zg-107	-7.72053	30.78954	NA	0.70	37.00	41.00	110.00	4.00	< 20	44.00	270.00
Zg-108	-7.72773	30.79094	NA	2.40	14.00	11.00	40.00	11.00	30.00	41.00	90.00
Zg-112	-7.75332	30.76962	NA	< 0.5	< 5	2.00	30.00	21.00	50.00	< 5	< 30
Zg-113	-7.75564	30.76921	NA	< 0.5	< 5	2.00	40.00	15.00	40.00	< 5	< 30
Imourkhssen area											
Im-2	-7.85856	30.93178	5	1.84	35.87	270.07	659.42	1486.51	20.57	84.53	17.68
Im-4	-7.85087	30.92966	20.50	< 1	22.15	62.72	72.57	20.00	20.84	39.52	56.55
Im-11	-7.87065	30.91878	11.20	< 1	166.91	104.53	450.27	16.52	22.34	31.08	19.67
Im-21	-7.85854	30.93179	29.77	8.69	35.60	92.84	1 439.88	12.32	18.16	58.17	24.03
Im-22	-7.86596	30.92166	22.5	1.42	42.98	44.25	675.43	< 10	44.96	82.82	130.30
Im-25	-7.86803	30.91663	11.20	< 1	< 20	81.73	65.80	< 10	22.19	50.55	68.05
Im-26	-7.86803	30.91663	8.00	< 1	25.65	125.97	34.41	< 10	14.54	31.88	13.99
Im-27	-7.86803	30.91663	16.00	< 1	20.81	174.74	28.71	< 10	17.61	32.17	12.93
Im-29	-7.86083	30.93011	16.00	< 1	32.55	51.28	57.94	< 10	35.58	41.01	57.02
Im-30	-7.86083	30.93011	8.00	< 1	34.26	59.39	149.86	< 10	34.78	44.98	66.13
Im-32	-7.8659	30.9216	4.80	< 1	30.21	58.10	20.80	< 10	22.02	42.16	88.42
Im-35	-7.86596	30.92166	4.80	< 1	24.15	106.33	25.98	< 10	17.81	41.67	34.91
Im-44	-7.86735	30.92038	4.80	< 1	< 20	113.10	16.47	19.34	16.98	21.74	27.60
Im-47	-7.86996	30.92021	4.80	< 1	< 20	177.83	12.61	108.72	8.99	22.03	7.25
Im-51	-7.87005	30.91785	4.80	< 1	< 20	46.82	40.48	< 10	18.23	42.77	117.35
Coordinates are in Decimal Degrees, ESPG:4326 – WGS 84 projection											

identifying 'blind' hydrothermal systems, where diagnostic argillic and phyllic alteration assemblages serve as indicators for deeper polymetallic potential (Tazi et al., 2026). Overall, the Siroua Massif remains poorly understood; extensive studies and characterization of its potential has been historically limited by land-tenure complexities and administrative constraints.

While previous research relied predominantly on traditional principal component analysis, these methods might often yield imprecise results due to manual component selection. Our study advances this by implementing a systematic numerical decision index that automates the identification and negation of mapping PCs based on diagnostic spectral contrasts (Supplementary Table). By integrating geochemical analysis with petrographic and mineralogical data, we bridge the gap between remote sensing theory and field reality, establishing a verifiable methodological framework for regional exploration.

Whereas our adopted numerical decision index on PCs significantly enhances the precision of spectral extraction, it is essential to define the operational boundaries of this methodology. Remote sensing remains an effective preliminary exploration tool and a guide for regional reconnaissance; however, it is not a substitute for traditional ground-based exploration, detailed geochemical sampling, or exploratory drilling. Moreover, the identification and interpretation of the detected alteration minerals via ASTER imagery

remains indirect and probabilistic, as spectral signatures can be influenced by surface weathering, biological crusts, or sub-pixel mineral mixing. Consequently, this approach is best framed as an early-stage exploration framework designed to narrow down vast terrains into high-priority targets. By integrating these remote sensing outputs with petrographic and geochemical studies, we mitigate these inherent uncertainties, transforming a probabilistic spectral model into a verifiable geological tool for the Siroua Massif.

CONCLUSIONS

This contribution focuses on the application of a selective PCA on ASTER data for hydrothermal alteration mapping and mineral targeting in the northern part of the Siroua Massif. On one hand, field investigations and petrographic studies of collected samples confirmed the presence and the spatial distribution of the alteration minerals mapped by the PCA technique. The evaluation confirmed that the ASTER VNIR-SWIR-TIR subsystems detect key alteration mineral assemblages. On the other hand, the anomalous concentrations of precious and base metals identified across both sectors significantly reinforce the economic potential of the study area.

The selective principal component analysis technique appeared to be an effective approach for delineating hydrothermal alteration zones, particularly evident given the arid to semi-arid conditions of the study area, where sparse and minimal vegetation cover facilitated a clearer spectral response. By employing this non-invasive technique, we identified key alteration signatures and polymetallic targets in the Zgounder mine and Imourkhssen areas. These results suggest that selective PCA remains a viable tool for preliminary mapping in similar geological settings. Nonetheless, multimodal integration of PCA with methods like band rationing, spectral angle mapper, and minimum noise fraction analysis is recommended for enhanced accuracy and spatial precision.

This green technology offers a sustainable method for mineral targeting, as it aligns with global standards for sustainable mining exploration, offering a non-invasive means for large-scale geological assessment with zero ecological impact.

Acknowledgements

Authors would like to thank the Zgounder Millennium Silver Mining Company (ZMSM), Aya Gold and Silver Group for accommodation and financial support during field work.

REFERENCES

1. Abati, J., Aghzer, A. M., Gerdes, A., & Ennih, N. (2010). Detrital zircon ages of neoproterozoic sequences of the Moroccan anti-atlas belt. *Precambrian Research*, *181*(1–4), 115–128. https://doi:10.1016/j.precamres.2010.05.018
2. Abrams, M. (2000). The Advanced Spaceborne Thermal Emission and Reflection Radiometer (ASTER): Data products for the high spatial resolution imager on NASA's Terra platform. *International Journal of Remote Sensing*, *21*(5), 847–859. https://doi.org/10.1080/014311600210326
3. Alvaro, J.J., Benziane, F., Thomas, R., Walsh, G.J., and Yazidi, A. (2014). Neoproterozoic–cambrian stratigraphic framework of the anti-atlas and Ouzellagh promontory (High Atlas), Morocco. *Journal of African Earth Sciences*, *98*, 19–33. https://doi:10.1016/j.jafrearsci.2014.04.026
4. Anderson, G.P., Felde, G.W., Hoke, M.L., Ratkowski, A.J., Cooley, T.W., Chetwynd Jr, J.H., and Lewis, P.E. (2002). August. MODTRAN4-Based atmospheric correction algorithm: FLAASH (Fast line-of-sight atmospheric analysis of spectral hypercubes). *Algorithms and Technologies for Multispectral, Hyperspectral, and Ultraspectral Imagery*, *8*(4725), 65–71. SPIE. https://doi.org/10.1117/12.478737
5. Bakardjiev, D., and Popov, K. (2015). ASTER spectral band ratios for detection of hydrothermal alterations and ore deposits in the Panagyurishte Ore Region, Central Srednogorie, Bulgaria. *Review of the Bulgarian Geological Society*, *76*(part 1), 79–88
6. Belkacim, S. (2014). *Petrology, geochemistry and Sr-Nd isotopes of Ediacaran volcanism and dolerite dykes of the Tifnoute Valley, and characterization of the Imourkhssen's Cu-Mo±Au occurrences (Siroua, Central Anti-Atlas, Morocco)*. Thesis, Ibn Zohr University, Morocco, 210 p (in French).
7. Bouougri, E. H., and Saquaque, A. (2004). Lithostratigraphic framework and correlation of the Neoproterozoic Northern West African Craton passive margin sequence (Siroua–Zenaga–Bouazzer Elgraara Inliers, Central Anti-Atlas, Morocco): an integrated approach. *Journal of African Earth Sciences*, *39*(3–5). 227–238. https://doi:10.1016/J.Jafrearsci.2004.07.045
8. Bouvart, T., Poot, J., Dekoninck, A., Schmit, F., De Greef, M. K., Vander Auwera, J., and Yans,

J. (2024). Alunite and kaolinite as geochemical markers in active acid sulfate alterations of southern Italy (Panarea, La Solfatara and Ischia). *Geochemistry*, *84*(4), 126204. https://doi.org/10.1016/j.chemer.2024.126204

9. Chattoraj, S.L., Prasad, G., Sharma, R.U., Van Der Meer, F.D., Guha, A., and Pour, A.B. (2020). Integration of remote sensing, gravity and geochemical data for exploration of Cu mineralization in Alwar Basin, Rajasthan, India. *International Journal of Applied Earth Observation and Geoinformation*, *91*, 102162. https://doi.org/10.1016/J.Jag.2020.102162
10. Crósta, A.P., and Moore, J.MCM. (1989). Enhancement of Landsat Thematic Mapper imagery for residual soil mapping in SW Minas Gerais State Brazil: A prospecting case history in greenstone belt terrain. *Proceedings of the 9th Thematic Conference on Remote Sensing for Exploration Geology, Calgary (Ann Arbor, MI: Environmental Research Institute of Michigan)*, 1173–1187.
11. Crósta, A.P., De Souza Filho, C.R., Azevedo, F., and Brodie, C. (2003). Targeting key alteration minerals in epithermal deposits in Patagonia, Argentina, using ASTER imagery and principal component analysis. *International Journal of Remote Sensing*, *24*(21), 4233–4240. https://doi:10.1080/0143116031000152291
12. Errami, E., Linnemann, U., Hofmann, M., Gärtner, A., Zieger, J., Gärtner, J., and Ennih, N. (2021a*). From Pan-African transpression to cadomian transtension at the West African margin: New U–Pb zircon ages from the Eastern Saghro Inlier* (*Anti-Atlas, Morocco*). Geological Society, London, Special Publications, *503*(1), 209–233. https://doi.org/10.1144/SP503-2020-105
13. Feng, L., Naz, I., Quddoos, A., Zafar, Z., Gan, M., Aslam, M., & Almutairi, K.F. (2025). Exploring rangeland dynamics in Punjab, Pakistan: Integrating LULC, LST, and remote sensing for ecosystem analysis (2000–2020). *Rangeland Ecology & Management*, *98*, 377–388. https://doi.org/10.1016/j.rama.2024.09.008
14. Gasquet, D., Ennih, N., Liégeois, J.P., Soulaimani, A., Michard, A. (2008). The Pan-African Belt. In: Michard, A., Saddiqi, O., Chalouan, A., Frizon De Lamotte, D. (Eds.). Continental evolution: The Geology of Morocco. *Lect. Notes Earth Sci*., *116*, 33–64. https://doi.org/10.1007/978-3-540-77076-3_2
15. Gasquet, D., Levresse, G., Cheilletz, A., Azizi-Samir, M.R., Mouttaqi, A. (2005). Contribution to a geodynamic reconstruction of the Anti-Atlas (Morocco) during Pan-African times with the emphasis on inversion tectonics and metallogenic activity at the Precambrian–Cambrian transition. *Precambrian Research*, 140(3-4), 157–182. https://doi:10.1016/J.Precamres.2005.06.009
16. Guglietta, D., Salzano, R., Wafik, A., Conte, A.M., Paciucci, M., Punturo, R., & Vaccaro, C. (2025). Hyperspectral investigation of an abandoned waste mining site: The Case of Sidi Bou Azzouz (Morocco). *Remote Sensing*, 17(11), 1838. https://doi.org/10.3390/rs17111838
17. Hedenquist, J.W., & Taran, Y.A. (2013). Modeling the formation of advanced argillic lithocaps: Volcanic vapor condensation above porphyry intrusions. *Economic Geology*, *108*(7), 1523–1540. https://doi.org/10.2113/econgeo.108.7.1523
18. Hodel, F., Triantafyllou, A., Berger, J., Macouin, M., Baele, J. M., Mattielli, N., and Poujol, M. (2020). The Moroccan Anti-Atlas ophiolites: timing and melting processes in an intra-oceanic arc-back-arc environment. *Gondwana Research*, 86, 182–202. https://doi.org/10.1016/J.Gr.2020.05.014
19. Iwasaki, A., and Tonooka, H. (2005). Validation of a crosstalk correction algorithm for ASTER/SWIR. *IEEE Transactions on Geoscience and Remote Sensing*, *43*(12), 2747–2751. https://doi:10.1109/TGRS.2005.855066
20. Kalkhoran, S.E., Ghannadpour, S.S., & Pour, A.B. (2025). Optimized hydrothermal alteration mapping in porphyry copper systems using a hybrid DWT-2D/MAD algorithm on ASTER satellite remote sensing imagery. *Minerals*, *15*(6), 626. https://doi.org/10.3390/min15060626
21. Laiche, M., Drissi, Y., Hinaje, S., Yaagoub, D., El Fartati, M., Ouahzizi, Y., & Laksir, A. (2025). Identification, genesis, and structural-gitological analysis of copper mineralization in the Middle Atlas, Morocco: integrating remote sensing with field investigations. *Journal of African Earth Sciences*, 105949. https://doi.org/10.1016/j.jafrearsci.2025.105949
22. Loughlin, W. (1991). Principal component analysis for alteration mapping. *Photogrammetric Engineering and Remote Sensing*, *57*, 1163–1169
23. Madani, A.A., and Emam, A.A. (2011). SWIR ASTER band ratios for lithological mapping and mineral exploration: A Case study from El Hudi Area, Southeastern Desert, Egypt. *Arabian Journal of Geosciences*, *4*(1). 45–52. https://doi:10.1007/S12517-009-0059-8
24. Marcoux, E., and Wadjinny, A. (2005). The Ag Hg Zgounder ore deposit (Jebel Siroua, Anti-Atlas, Morocco): A neoproterozoic epithermal mineralization of the Imiter type. *Comptes Rendus Geoscience*, *337*(16), 1439–1446. https://10.1016/j.crte.2005.09.005
25. Mars, J.C., and Rowan, L.C. (2006). Regional mapping of phyllic-and argillic-altered rocks in the Zagros magmatic arc, Iran, using advanced spaceborne thermal emission and reflection radiometer (ASTER) data and logical operator algorithms. *Geosphere*, *2*(3), 161–186. https://doi.org/10.1130/GES00044.1

26. Moore, F., Rastmanesh, F., Asadi, H., and Modabberi, S. (2008). Mapping mineralogical alteration using principal-component analysis and matched filter processing in the Takab Area, North-West Iran, From ASTER Data. *International Journal of Remote Sensing*, *29*(10), 2851–2867. https://doi:10.1080/01431160701418989
27. Neal, L.C., Wilkinson, J.J., Mason, P.J., and Chang, Z. (2018). Spectral characteristics of propylitic alteration minerals as a vectoring tool for porphyry copper deposits. *Journal of Geochemical Exploration*, *184*, 179–198. https://doi.org/10.1016/j.gexplo.2017.10.019
28. Ninomiya, Y., and Fu, B. (2016). Regional lithological mapping using ASTER-TIR Data: Case study for the Tibetan plateau and the surrounding area. https://doi.org/10.3390/geosciences6030039
29. Orynbassarova, E., Ahmadi, H., Adebiyet, B., Bekbotayeva, A., Abdullayeva, T., Beiranvand Pour, A., and Bermukhanova, A. (2025). Mapping alteration minerals associated with aktogay porphyry copper mineralization in eastern Kazakhstan using Landsat-8 and ASTER satellite sensors. *Minerals*, *15*(3), 277. https://doi.org/10.3390/min15030277
30. Oukassou, M. (2013). *Vertical movements of the northern border of the West African Craton (Central Anti-Atlas, Morocco): Contribution of low temperature thermochronology*. Thesis, Hassan II University, Casablanca, Morocco, 139P. (in French)
31. Pelleter, E., Cheilletz, A., Gasquet, D., Mouttaqi, A., Annich, M., Camus, Q., and Ouchtouban, L. (2016). U/Pb ages of magmatism in the zgounder epithermal Ag–Hg deposit, Sirwa Window, Anti-Atlas, Morocco. *In Mineral Deposits of North Africa* (pp. 143–165). Cham: Springer International Publishing. https://doi:10.1007/978-3-319-31733-5_5
32. Pour, A.B., Hashim, M., Hong, J. K., and Park, Y. (2017). Lithological and Alteration Mineral Mapping in poorly exposed lithologies using Landsat-8 And ASTER satellite data: North-Eastern Graham Land, Antarctic Peninsula. *Ore Geology Reviews*, *108*, 112–133. https://doi.org/10.1016/j.oregeorev.2017.07.018
33. Pour, A.B., and Hashim, M. (2012). The application of ASTER remote sensing data to porphyry copper and epithermal gold deposits. *Ore Geology Reviews*, *44*, 1–9. https://doi.org/10.1016/j.oregeorev.2011.09.009
34. Rowan, L.C., Schmidt, R.G., and Mars, J.C. (2006). Distribution of hydrothermally altered rocks in the Reko Diq, Pakistan mineralized area based on spectral analysis of ASTER Data. *Remote Sensing of Environment*, *104*(1), 74–87. https://doi.org/10.1016/J.Rse.2006.05.014
35. Tazi, M.J., Ouchchen, M., El Azzab, D., Benyahia, D., Bajadi, A., Boufakri, H., & Dadi, B. (2026). Integration of ASTER remote sensing and gamma-ray spectrometry for mapping hydrothermal alteration in the Sirwa Massif, Central Anti-Atlas, Morocco: A guide for mining exploration. *Journal of African Earth Sciences*, 106019. https://doi.org/10.1016/j.jafrearsci.2026.106019
36. Thomas, R.J., Fekkak, A., Ennih, N., Errami, E., Loughlin, S.C., Gresse, P.G., Liégeois, J.P. (2004). A new lithostratigraphic framework for the Anti-Atlas Orogen, Morocco. *Journal of African Earth Sciences*, *39*(3–5), 217–226. https://doi:10.1016/J.Jafrearsci.2004.07.046
37. Thomas, R.J., Chevallier, L.P., Gresse, P.G., Harmer, R.E., Eglington, B.M., Armstrong, R.A., De Beer, C.H., et al. (2002). Precambrian evolution of the Sirwa window, Anti-Atlas Orogen, Morocco. *Precambrian Research*, *118*(1–2), 1–57. https://doi:10.1016/S0301-9268(02)00075-X
38. Toummite, A. (2012). *Terminal proterozoic granitoids of the Tifnoute Valley Region (Anti-Atlas). An example of post-collisional magmatism of juvenile origin in a Metacratonic Context. Geochemistry - Geochronology - Sr-Nd Isotopes*. Thesis, Ibn Zohr University, Morocco, 183p. (in French)
39. Toummite, A., Liégeois, J.P., Gasquet, D., Bruguier, O., Beraaouz, E.H., and Ikenne, M. (2013). Field, geochemistry and Sr-Nd isotopes of the Pan-African granitoids from the Tifnoute Valley (Sirwa, Anti-Atlas, Morocco): A post-collisional event in a metacratonic setting. *Mineralogy and Petrology*, *107*(5), 739–763. https://doi.org/10.1007/s00710-012-0245-3
40. Tuduri, J., Chauvet, A., Barbanson, L., Bourdier, J. L., Labriki, M., Ennaciri, A., and Maacha, L. (2018). The jbel Saghro Au (–Ag, Cu) and Ag–Hg metallogenetic province: Product of a long-lived Ediacaran tectonomagmatic evolution in the Moroccan Anti-Atlas. *Minerals*, *8*(12), 592. https://doi.org/10.3390/min8120592
41. Wambo, J.D.T., Pour, A.B., Ganno, S., Asimow, P.D., Zoheir, B., dos Reis Salles, R., & Muslim, A.M. (2020). Identifying high potential zones of gold mineralization in a sub-tropical region using Landsat-8 and ASTER remote sensing data: a case study of the Ngoura-Colomines goldfield, eastern Cameroon. *Ore Geology Reviews*, *122*, 103530. https://doi.org/10.1016/j.oregeorev.2020.103530
42. Zerai, F.T., Gorsevski, P.V., Panter, K.S., Farver, J., and Tangestani, M.H. (2023). Integration of ASTER and soil survey data by principal components analysis and one-class support vector machine for mineral prospectivity mapping in Kerkasha, Southwestern Eritrea. *Natural Resources Research*, 32(6), 2463–2493. https://doi.org/10.1007/s11053-023-10268-3